

Modeling Mergers of Known Galactic Systems of Binary Neutron Stars

Alessandra Feo,¹ Roberto De Pietri,¹ Francesco Maione,¹ and Frank Löffler²

¹*Parma University and INFN Parma, Parco Area delle Scienze 7/A, I-43124 Parma (PR), Italy*

²*Center for Computation & Technology, Louisiana State University, Baton Rouge, LA 70803 USA*

(Dated: August 3, 2018)

We present a study of the merger of six different known galactic systems of binary neutron stars (BNS) of unequal mass with a mass ratio between 0.75 and 0.99. Specifically, these systems are J1756-2251, J0737-3039A, J1906+0746, B1534+12, J0453+1559 and B1913+16. We follow the dynamics of the merger from the late stage of the inspiral process up to ~ 20 ms after the system has merged, either to form a hyper-massive neutron star (NS) or a rotating black hole (BH), using a semi-realistic equation of state (EOS), namely the seven-segment piece-wise polytropic SLy with a thermal component. For the most extreme of these systems ($q = 0.75$, J0453+1559), we also investigate the effects of different EOSs: APR4, H4, and MS1. Our numerical simulations are performed using only publicly available open source code such as, the Einstein Toolkit code deployed for the dynamical evolution and the LORENE code for the generation of the initial models. We show results on the gravitational wave signals, spectrogram and frequencies of the BNS after the merger and the BH properties in the two cases in which the system collapse within the simulated time.

PACS numbers: 04.25.D-, 04.40.Dg, 95.30.Lz, 97.60.Jd

I. INTRODUCTION

The direct observation of the gravitational wave (GW) signal in events GW150914 and GW151226 [1, 2], emitted by the coalescence of a compact binary system composed by two black holes (BH) is the dawn of the GW astronomy era. The measured signal from those events shows the expected signature of an inspiral and merger, and subsequent final black hole ringdown. This single event encourages further studies of properties and astrophysical implications of binary black hole (BBH) populations [3, 4]. Among compact binary systems, binary neutron star (BNS) mergers are another expected source candidate for GW astronomy. Their composition and ultra-dense neutron star (NS) matter behavior encoded in the Equation of State (EOS) make them a unique target to be measured with ground-based interferometers (Advanced LIGO [5], Advanced Virgo [6], and KAGRA [7]), in order to understand the structure and properties of NS systems and the distribution of NS masses.

The first BNS system discovered is PSR B1913+16, better known as Hulse-Taylor binary [8], a pulsar which, together with another NS is in orbit around a common center of mass forming a binary star system. This system provided indirect evidence of the emission of GW as predicted by General Relativity [8, 9] (from now on we will use the pulsar name to denote the corresponding BNS system). Since then, nine other binary neutron star systems have been discovered in our galaxy (see Ref. [10] for details). Among them is also the binary system of the pulsar J0453+1559 [10], with a mass ratio of ($q = M_1/M_2 = 0.75$) [10], confirming the existence of unequal mass BNS systems in nature with a quite unexpected large mass difference between the two stars. This fact has the potential to change and improve our understanding on the nature of NS formation as well as their evolution and final fate. Because of this, it also should

be considered when computing templates of GW signals from BNS mergers for data analysis pipelines.

In this paper we analyze all known BNS systems in our galaxy for which both masses are known (see Table I [10]). They contain both the recently discovered system J0453+1559 ($q = 0.75$) [10], as well as J0737-3039A, which is the most relativistic binary BNS known today [12, 13] and the only binary pulsar. Driven by the experimental discovery of a $q = 0.75$ BNS, we present three-dimensional numerical simulations of the dynamics of BNS mergers with different total baryonic mass and different mass ratio up to $q = 0.75$, to understand the impact of the mass ratio on the GW signal emitted in both the last orbits before merger and in the post-merger phase. For all systems, we use the SLy EOS [20], based on the Skyrme Lyon effective nuclear interaction, where a semi-realistic seven-segment piece-wise (isentropic)-polytropic approximant [21] is implemented, namely the SLyPP EOS, including a thermal component given by $\Gamma_{th} = 1.8$. We use the BSSN-NOK [22–26] method for the evolution of the gravitational sector and WENO [27] as a reconstruction method for the matter sector. This study has been performed using only publicly available open source software, in particular, the Einstein Toolkit (ET) [28, 29], used for the dynamical evolution, and the LORENE code [30, 31] to generate the initial models, similar to studies recently published in Refs. [32, 33].

For the most extreme model, the J0453+1559 system ($q = 0.75$), we also investigate the effects of using different EOS for nuclear matter, which include: the APR4 EOS [34], the H4 EOS [35] and the MS1 EOS [36].

The organization of the paper is as follows. In Sec. II we briefly review the numerical setup used. A detailed discussion of an essentially identical setup can be found in [32]. In Sec. III, we discuss each of the models and present the results of our simulations: the fate of these

Pulsar	M_p (M_\odot)	M_c (M_\odot)	q	e	t_{merger} (Gyr)	e_{10} at 10 Hz	$M^{(1)}$ (M_\odot)	$M^{(2)}$ (M_\odot)	e_{ID}	Ω (krad/s)	M_{ADM} (M_\odot)	J (GM_\odot^2/c)	Reference
J1756-2251	1.341(7)	1.230(7)	0.92	0.18056	15.85	7.20×10^{-7}	1.33	1.47	0.022	1.773	2.548	6.654	[11]
J0737-3039A	1.3381(7)	1.2489(7)	0.93	0.08778	0.08	1.11×10^{-6}	1.36	1.47	0.023	1.777	2.564	6.728	[12, 13]
J1906+0746	1.291(11)	1.322(11)	0.98	0.08530	0.32	6.48×10^{-7}	1.41	1.45	0.024	1.784	2.589	6.848	[14, 15]
B1534+12	1.3330(2)	1.3454(2)	0.99	0.27368	2.51	8.85×10^{-8}	1.46	1.47	0.025	1.801	2.653	7.136	[16, 17]
J0453+1559	1.559(5)	1.174(4)	0.75	0.11252	14.55	1.14×10^{-8}	1.27	1.74	0.030	1.816	2.708	7.238	[10]
B1913+16	1.4398(2)	1.3886(2)	0.96	0.61713	0.32	5.32×10^{-6}	1.53	1.59	0.025	1.840	2.801	7.816	[8, 9]

TABLE I. Known BNSs in our galaxy, as appearing in Ref.[10]. M_p is the mass of the pulsar that denotes the system and M_c the mass of its companion, q represents the mass ratio, and e the eccentricity. t_{merger} is the merger time of the system computed using Eq. (7) of [18], and e_{10} is the eccentricity when the rotation frequency of the system is 10 Hz, computed using Eq. (1.2) of [19]. The remaining columns represent the properties of the initial data used to model the BNS system using the SLy EOS, where $M^{(1)}$ and $M^{(2)}$ are the baryonic masses, e_{ID} is the measured eccentricity, Ω the initial rotation frequency, M_{ADM} the ADM mass of the system and J its angular momentum.

systems, the properties of the remnants, and the effect of the EOS for the case of J0453+1559. A summary and conclusions are given in Sec. IV.

In this work we use a space-like signature $- , + , + , +$, with Greek indices running from 0 to 3, Latin indices from 1 to 3, and the standard convention for summation over repeated indices. The computations are performed using the standard $3+1$ split into (usually) space-like coordinates $(x, y, z) = x^i$ and a time-like coordinate t . Our coordinate system $(x^\mu) = (t, x^i) = (t, x, y, z)$ (far-from the origin) are, as it can be checked, almost isotropic coordinates and (far-from the origin) they would have the usual measure unit of “time” and “space” and in particular t is close to be identified as the time measured from an observer at infinity. All computations are performed in normalized computational units (hereafter denoted as CU) in which $c = G = M_\odot = 1$. We report the radius of the sphere used for gravitational waves extraction in CUs.

II. NUMERICAL SETUP

The systems analyzed in this paper share a similar dynamics pre-merger: an inspiral driven by gravitational wave radiation. We follow the remnant of the merger for approximately 20 ms post-merger to determine its properties, and to be able to measure gravitational waves leaving the system. As will be shown in Sec. III, some of these collapse to a BH, requiring a black hole horizon finder.

We have analyzed similar models in the past for ad-hoc system parameters. The same numerical setup can be used for the current study, which is why we will only briefly summarize the setup here and refer the reader to Ref. [32] for details. One fundamental aspect of the present study is that all data has been produced using only freely available, open source software. Moreover, all information necessary to reproduce and re-analyze our simulations has been made available in the same way. Detailed instruction on how to achieve this can be found on the Subversion server of the gravity group at Parma

University.

In order to describe BNS systems we need to use the Einstein’s general relativity equations to describe the metric $g_{\mu\nu}$ of the dynamical spacetime

$$R_{\mu\nu} - \frac{1}{2}g_{\mu\nu}R = \frac{8\pi G}{c^4}T_{\mu\nu}. \quad (1)$$

The dynamical evolution is described using the Einstein Toolkit, which is a publicly available, community-driven general relativistic code. In particular, we have chosen the eleventh release (code name “Hilbert”, ET_2015_05). The ET is based on the Cactus computational toolkit [37–39], a software for high performance computing that uses: the adaptive mesh refinement (AMR) methods implemented by Carpet [40–42]. In particular, the initial data is discretized on a Cartesian grid with 6 levels of mesh refinement. The inner level contains a grid with a spacing of $dx = 0.25$ CU that corresponds to $\simeq 369$ m. We also use a mirror symmetry across the (x,y) plane which reduces the computational cost of the simulations by a factor of 2. The evolution of the spacetime metric is managed using the McLachlan package [43], and more specifically the version implementing the Einstein equations through a $3+1$ dimensional split using the BSSN-NOK formalism, where we use a fourth order finite difference stencils for the curvature evolution and a Γ -driver shift condition [26]. During evolution, a Sommerfeld-type radiative boundary condition is applied to all components of the evolved BSSN-NOK variables as described in [25], and the HLLC (Harten-Lax-van Leer-Einfeldt) approximate Riemann solver [44, 45] is used. The initial data of our simulations are generated using the LORENE code [30] and in particular, we use the irrotational BNS data generation of [31].

We also need a proper description of matter (details can be found in Ref. [32]). In particular, we use the energy-momentum tensor $T_{\mu\nu}$ to be that of an ideal relativistic fluid: $T^{\mu\nu} = \rho(1 + \epsilon + \frac{p}{\rho})u^\mu u^\nu + Pg^{\mu\nu}$, where ρ is the rest mass density, ϵ is the specific internal matter energy, u^μ is the 4-velocity of the matter and P is the pressure. We also use the conservation laws for the energy-

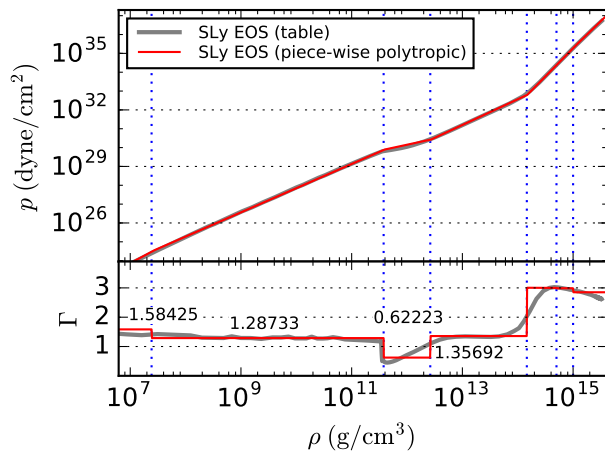


FIG. 1. Plot of the pressure (p) and of the adiabatic index ($\Gamma = d\log(p)/d\log(\rho)$) as a function of the baryon density (ρ) for the SLy EOS (tabulated) and its piece-wise polytropic approximation (the one used in the present work).

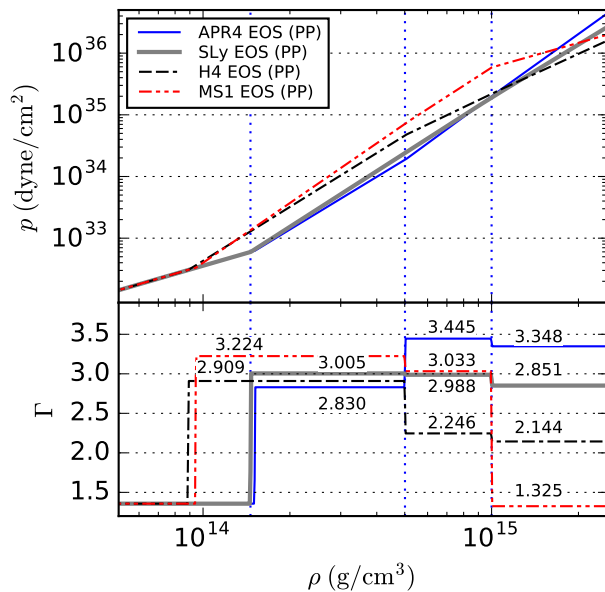


FIG. 2. Plot of the pressure (p) and of the adiabatic index ($\Gamma = d\log(p)/d\log(\rho)$) as a function of the baryon density (ρ) for the SLy EOS piece-wise polytropic approximation (the same used in Fig.1) together with the APR4, H4 and MS1 EOSs.

momentum tensor, $\nabla_\mu T^{\mu\nu} = 0$ and the baryon density $\nabla_\mu(\rho u^\mu) = 0$, closed by an EOS of the type $P = P(\rho, \epsilon)$.

For all the BNS models investigated in this paper, we use, unless otherwise stated, a seven-segment isentropic polytropic approximant, that we refer as SLyPP, and that was already used in our previous work [32]. This EOS belongs to the SLy EOS prescription [20], supplemented by a thermal component $\Gamma_{\text{th}} = 1.8$ (details can be found in [32]). In particular, we use four pieces for the crust and three pieces for the core [21]. The EOS is

described through the expression

$$P(\rho, \epsilon) = P_{\text{cold}}(\rho) + P_{\text{th}}(\rho, \epsilon), \quad (2)$$

where each density region, $\rho_i \leq \rho < \rho_{i+1}$, satisfy:

$$P_{\text{cold}} = K_i \rho^{\Gamma_i}, \quad (3)$$

$$\epsilon_{\text{cold}} = \epsilon_i + \frac{K_i}{\Gamma_i - 1} \rho^{\Gamma_i - 1} \quad (4)$$

and ϵ_i and the polytropic constant K_i are chosen to guarantee the pressure and specific energy density continuity.

During the evolution, the EOS of the cold nuclear matter is supplemented by a thermal component of the form:

$$P_{\text{th}} = \Gamma_{\text{th}} \rho (\epsilon - \epsilon_{\text{cold}}) \quad (5)$$

and choosing Γ_{th} , as in our previous work [32, 33], to be 1.8 according to [46–49]. Fig. 1 shows a plot of the pressure p and the adiabatic index $\Gamma = \frac{d\log(p)}{d\log(\rho)}$ as a function of the baryonic density ρ for the SLy EOS (gray line) [20] and its piece-wise polytropic SLy EOS (red line) [21].

For the more extreme system ($q = 0.75$, J0453+1559), beside the study of the SLy EOS, we also investigate the effects of assuming other cold EOSs for nuclear matter at beta equilibrium. Summarizing, we analyzed in decreasing order of compactness:

- The APR4 EOS [34], obtained using variational chain summation methods using the Argonne two-nucleon interaction and also including boost corrections and three-nucleon interactions;
- The SLy EOS [20], based on the Skyrme Lyon effective nuclear interactions;
- The H4 EOS [35], constructed in a relativistic mean field framework including also Hyperons contributions and tuning the parameters to have the possible stiffest EOS compatible with astrophysical data;
- The MS1 EOS [36], constructed with relativistic means field theory considering only standard nuclear matter.

We show in Fig. 2 the core part of Fig. 1 but for all the different EOS used, namely: APR4, H4, MS1 and the SLy EOSs. Notice, that up to a baryonic density of the order of $10^{14} \text{ g cm}^{-3}$, which represents the separation between the crust and the core of the NS, we use the same prescription: the one coming from the prescription of the crust given in Ref. [20] using the parametrization of Ref. [21].

III. RESULTS

We have analyzed the dynamics of the merger of six different BNS systems, that appear in Table I, from

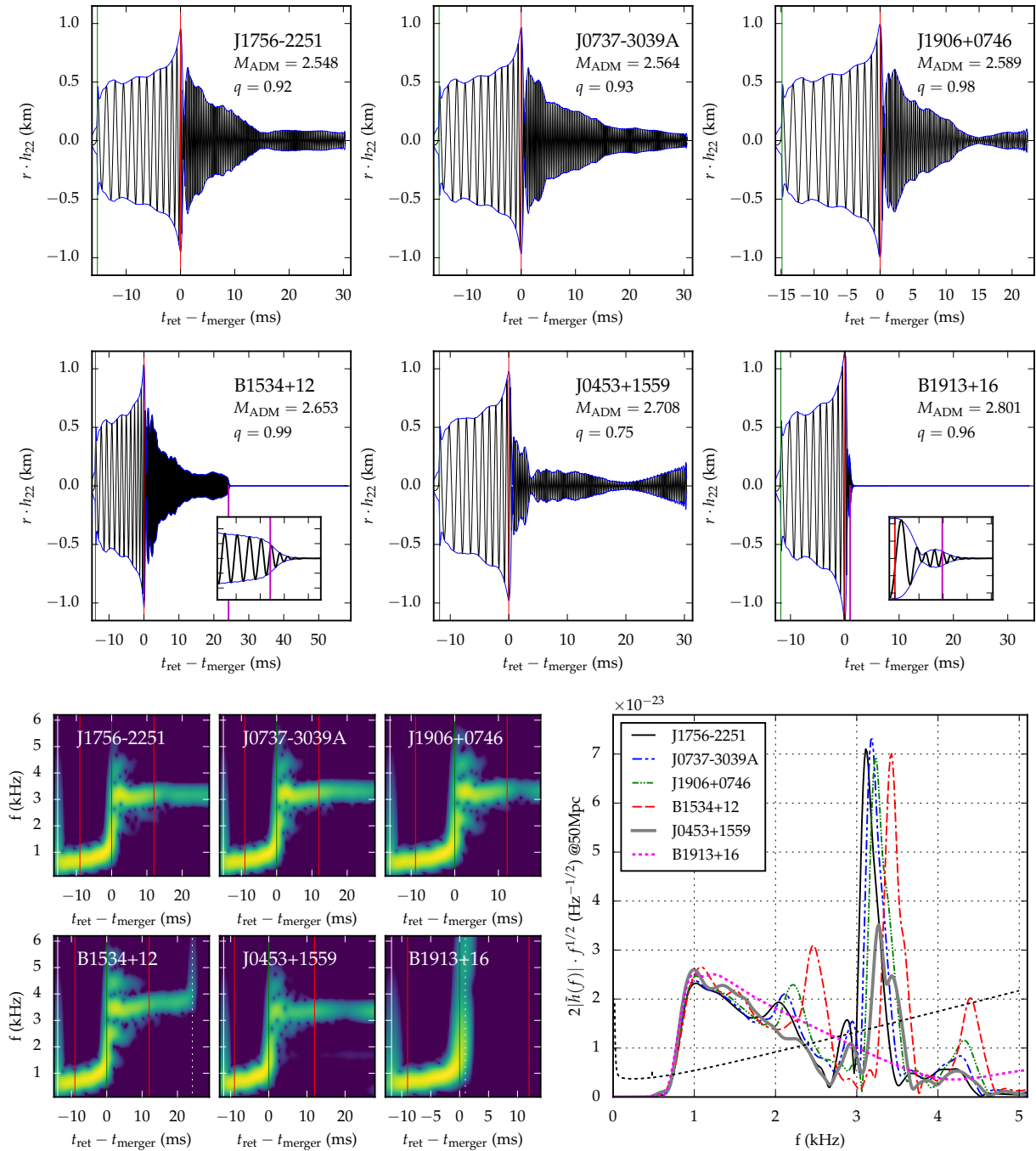


FIG. 3. Overview of the models studied using the SLy EOS. These models are J0453+1559, J1756-2251, J0737-3039A, B1913+16, J1906+0746, B1534+12, with unequal mass ratios of $q = 0.75, 0.92, 0.93, 0.96, 0.98, 0.99$, respectively. We report in the top panel the amplitudes of the main $l = 2, m = 2$ mode of the gravitational wave signal, and in the bottom-left panel the corresponding spectrogram. In the bottom-right panel we show the corresponding power spectral density for the six systems at a distance of 50 Mpc, where the Fourier transform is computed on the interval going from 9 ms before merger to 12 ms after merger.

the late-inspiral phase (last five-six orbits, depending on the model) until approximately 20 ms after merger. These models are J0453+1559, J1756-2251, J0737-3039A, B1913+16, J1906+0746, B1534+12, with an unequal mass ratio of $q = 0.75, 0.92, 0.93, 0.96, 0.98, 0.99$, respectively. In the following, we present the general

characteristics of the evolution of these systems.

We extracted the gravitational wave (GW) signal from each simulation using the same procedure of Ref. [33]. In brief, for each simulation we extracted the GW signal from the curvature ψ_4 [50, 51], written in terms of spin-

weighted spherical harmonics of spin -2 [52]:

$$\psi_4(t, r, \theta, \phi) = \sum_{l=2}^{\infty} \sum_{m=-l}^l \psi_4^{lm}(t, r) {}_{-2}Y_{lm}(\theta, \phi) \quad (6)$$

up to $l = 6$. At null infinity, ψ_4 is related to the GW strain through the relation

$$\psi_4 = \ddot{h}_+ - i\ddot{h}_x := \ddot{\bar{h}}, \quad (7)$$

where \bar{h} is the complex conjugation of the GW strain. To get the GW strain components h^{lm} , we numerically integrate this expression twice

$$\bar{h}_{lm}^{(0)} = \int_0^t dt' \int_0^{t'} dt'' \psi_4^{lm}(t'', r) \quad (8)$$

$$\bar{h}_{lm} = \bar{h}_{lm}^{(0)} - Q_1 t - Q_0 \quad (9)$$

and we fix the two initial values of the integration procedure (Q_0 and Q_1) by minimizing the overall drifting. However, it is well known that this procedure still shows low-frequency spurious oscillations in the strain amplitude. As discussed in [33], we remove this (quite likely due to noise aliasing problems) by applying, after the integration and the subtraction of the linear drift, a digital high-pass Butterworth filter (an IIR filter) imposing a maximum signal suppression of -0.01 dB at the minimum physical frequency $f_0 = \Omega/\pi$ (computed as twice the initial orbital frequency) and a signal suppression of -80 dB at $f_0/10$.

In this work we extracted the GW signal at the coordinate radius of $R = 700$ CU (1034 km) and we always report the retarded time (for GW extraction quantities) that corresponds to the coordinate time for quantities integrated over the numerical grid. In detail, we have $t_{\text{ret}} = t - R^*$, ($R^* = R + 2M_{\text{ADM}} \log(-1 + R/2M_{\text{ADM}})$) since our numerical relativity coordinate system far away from the center is almost identical to isotropic coordinates. We also implement a 1st order extrapolation in $1/R$, as proposed in [53] (see [33] for details).

To obtain the energy and the angular momentum budgets of the collapsed models we used the energy E_{gw} and the angular momentum J_{gw} carried away by GW, which are given by

$$\frac{E_{\text{gw}}}{dt} = \frac{R^2}{16\pi} \int d\Omega |\dot{h}(t, \theta, \phi)|^2, \quad (10)$$

$$\frac{dJ_z^{\text{gw}}}{dt} = \frac{R^2}{16\pi} \text{Re} \left[\int d\Omega \left(\partial_\phi \dot{h}(t, \theta, \phi) \right) h(t, \theta, \phi) \right], \quad (11)$$

as well as the mass M_{bh} and angular momentum of the BH J_{bh} , computed using the isolated horizon formalism [54–56] on the apparent horizon, utilizing the ET modules `QuasilocalMeasures` [57] and `AHFinderDirect` [58]. The mass and angular momentum contribution of matter is defined in [32].

A. Properties of the six galactic binary neutron star systems

The overview of the evolution of known Galactic systems of BNS is presented in Fig.3, where we show the amplitude of the $r \cdot h_{22}$ mode as a function of $(t - t_{\text{merger}})$ (top), the spectrum of frequencies (spectrogram) using 5 ms bins as a function of the time (on the bottom-left panel), and the power spectral density (PSD, Fourier Transform) of the effective GW $\bar{h}(f)$, in the optimal oriented case for a source at 50 Mpc, where we consider the signal from 9 ms before, to 12 ms after merger in the bottom-right panel.

The evolution of the six galactic systems on top of Fig.3 is shown in the order of increasing ADM mass. All these models used the SLy EOS and an interbinary distance of 44.3 km. All the numerical simulations presented in this paper were performed with a resolution of $dx = 0.25$ CU which corresponds to $\simeq 369$ m). The green line in each BNS represents $t_{\text{ret}} = 0$. The red line indicates the merger time at $t = 0$ ms. We define merger time here as the time of maximal GW signal amplitude.

An additional purple line shows the formation of a BH and only appears for two of these systems (B1913+16 and B1534+12), at least during the simulation time we have investigated. These two pulsars show-case two different merger remnants involving a BH. B1913+16 (the Hulse-Taylor binary) rapidly collapses to a BH, while B1534+12 shows a delayed collapse to a BH a few milliseconds after the merger (around 25 ms in this particular simulation). For both of these systems, we increased the simulation time up to 40 ms after merger to analyze the formation of an accretion disk (see section III B for details).

Model J0453+1559, with an ADM mass in between the masses of B1534+12 and B1913+16, does not collapse to a BH during the simulated time (around 30 ms after merger). This is probably related to the fact that it corresponds to an extreme unequal mass system (with $q = 0.75$), while the other two pulsars, that do collapse to a BH, have almost equal masses. The remaining models (see Table I) form a remnant lasting more than 20 ms after merger. All of them will eventually collapse to a BH since their masses are greater than the maximum mass that can be supported by the SLy EOS for a uniformly rotating star. We did not follow up on those stages in this paper.

The PSD of the effective GW signal in Fig.3 (bottom-right panel) shows the presence of a dominating peak for each model, except for the one that rapidly collapses to a BH (B1913+16). This peak corresponds to the frequency f_p (also called f_2 or f_{peak}) of the fundamental quadrupolar $m = 2$ oscillation mode of the massive NS formed after the merger [59], and depends on the compactness of the star [47, 49, 60–62]. This dependence can be seen in our data as increase of f_p for more compact systems, within a range of 3 kHz to 4 kHz for models J1756-2251, J0737-3039A, J1906+0746 and B1534+12, where B1534+12 has the largest ADM mass. The only exception is B1913+16,

Model	τ_0 (ms)	f_0 (kHz)	f_p (kHz)	\hat{f}_p (kHz)	f_- (kHz)	f_+ (kHz)
J1756-2251	2.49	1.148	3.163	3.114	2.028	4.280
J0737-3039A	2.74	1.139	3.293	3.182	2.105	4.271
J1906+0746	2.72	1.119	3.326	3.231	2.206	4.321
B1534+12	3.72	0.984	3.667	3.424	2.459	4.397
J0453+1559	2.54	0.998	3.331	3.268	—	—

TABLE II. Main peak frequencies and damping times of the post-merger phase of the simulated models at $dx = 0.25$ CU. τ_0 and f_0 are the dumping time and the frequency of the oscillation of the lapse α between 1.5 to 8 ms after t_{merger} , respectively. The frequency f_p is determined by a single-frequency fitting procedure on the last part of h_{22} signal. The frequencies, \hat{f}_p , f_- , f_+ , are derived by an analysis of the Fourier spectrum and represent the frequencies of the main and secondary peaks of the PSD (bottom-right panel of Fig. 3). Notice that we do not include the sixth galactic system (B1913+16) as it rapidly goes to a BH.

whose PSD rapidly decays to zero as the pulsar collapses to a BH soon after the merger. Also, J0453+1559 does not follow this trend due to its very low $q = 0.75$ value, which renders this system quite different from the others.

Some of the models show other, secondary post-mergers peaks at frequencies f_- and f_+ (also known as f_1 and f_3 in the literature) that can be seen in Fig.3. They are also recognizable from the spectrum and may help to extract NS parameters (radius, mass) from GW detections [63, 64]. In Table II we report the frequencies of all recognizable spectral peaks for the BNS systems of Fig. 3.

One of the systems clearly exhibiting these three peaks is B1534+12, with the middle peak f_p and two secondary peaks in both sides of the principal frequency. The same three peaks can be observed for models J1756-2251, J0737-3039A and J1909+0746. See Table II for their specific frequencies. It should be noted that the secondary peaks f_{\pm} decays within few ms as it can be seen in the spectrograms (bottom-left) of Fig. 3.

On the other hand, this three-peak-structure does not show up in the case of the J0453+1559 ($q = 0.75$). This is consistent with the results of Ref. [32], where it has been shown that the three-peak-structure is gradually suppressed for unequal mass BNS systems. A similar behavior (suppression of peaks) can be observed analyzing the same system using another EOS (see Section III C for more details). Moreover, for the J0453+1559 system it should be noted that there is a small shift of frequency, 22 ms after the merger, and that the mode is growing with a characteristic exponential growth time of $\tau = 5.75$ ms and a frequency equal to $f_p = 3.331$ kHz. This growing amplitude suggests the activation of an unstable mode. A similar phenomenon is also present for the J1906+0746 system, where 15 ms after the merger a growing mode with $f_p = 3.329$ kHz and $\tau = 5.30$ ms is observed. On the other hand, growing modes are not present for J1756-2251 and 0737-3039A. The presence of such instabilities of the remnant should not be considered unexpected,

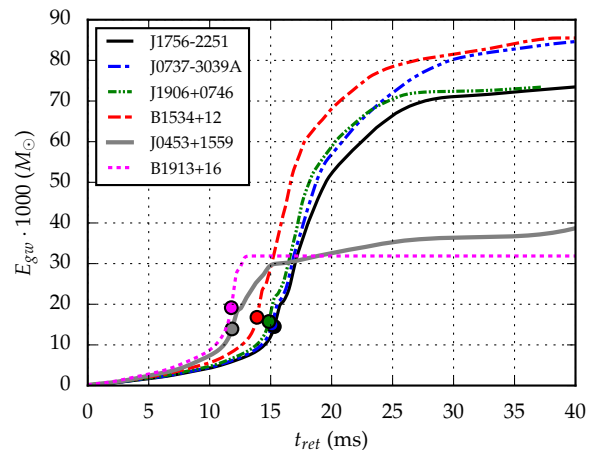


FIG. 4. Evolution of the total energy momentum (E_{gw}) carried away by gravitational radiation in solar mass as a function of the retarded time t_{ret} , for the six different BNS models. The colored circles mark the merger time for each model as indicated in Table III.

Model	E_{gw} (M_{\odot}) [...-5]	E_{gw} (M_{\odot}) [-5...5]	E_{gw} (M_{\odot}) [5...20]	t_{merger} (ms)
J1756-2251	0.0276	0.0488	0.0189	15.3
J0737-3039A	0.0277	0.0528	0.0255	15.1
J1906+0746	0.0282	0.0582	0.0148	14.0
B1534+12	0.0297	0.0597	0.0192	13.9
J0453+1559	0.0287	0.0269	0.0060	11.8
B1913+16	0.0317	0.0276	$6 \cdot 10^{-7}$	11.8

TABLE III. For each model is reported the total energy emitted as gravitational waves from infinite separation up to 5 ms before merger (second column), from 5 ms before merger up to 5 ms after merger (third column) and from 5 ms after merger up to 20 ms after merger (forth column). In the fifth column is reported the merger time in ms. All these values refer to simulations performed with resolution $dx = 0.25$ CU (≈ 369 m).

since it is well known that differentially rotating stars show dynamical instabilities, and that the threshold for their activation depends on the EOS (see [65–69] and reference therein).

In addition to hydrodynamical quantities, we also analyzed the gravitational waves generated by such encounters. Fig. 4 shows the total energy momentum (E_{gw}) that is carried away by gravitational radiation as a function of the retarded time $t = t_{\text{ret}}$, for all six different BNS models. As can be seen from this figure, the total energy momentum carried away by GWs starts increasing only slowly at first, goes through a burst of radiation and then approaches a more or less steady value in the post-merger region at approximately 20 ms after merger. For this reason, we report for each system the total emitted gravitational energy for three different time intervals in Table III. From infinite separation up to 5 ms before merger (inspiral phase), from 5 ms before merger up to 5 ms after merger (merger phase) and from 5 ms after

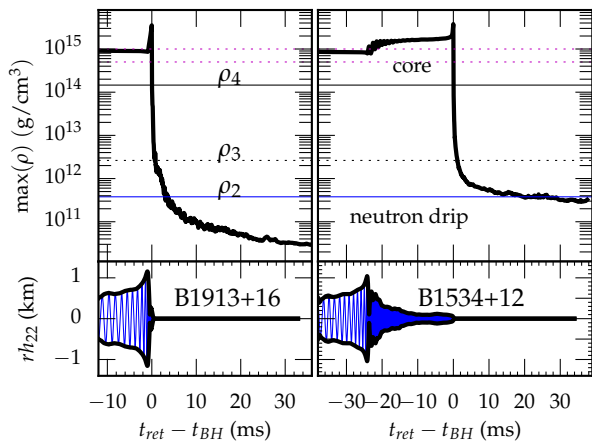


FIG. 5. Evolution of the maximum baryonic density as a function of time for the evolution of systems B1913+16 (left) and B1534+12 (right). Bottom panel: GW envelope waves emitted by both systems. Notice that the maximum density (on the whole numerical grid) quickly drops below the neutron drip density just after the formation of the BH ring-down.

merger up to 20 ms after merger (post-merger phase). As can be seen, the total amount of emitted energy is not much different for all models in the inspiral phase. The same it is true for the merger phase, except for the B1913+16 system that promptly collapses, forms a BH, and thus reduces GW emission noticeably just after the merger. Another exception is the more extreme unequal mass ($q = 0.75$) J0453+1559 system, which shows a noticeably lower emission. This is in accordance with results in [32], where it was also observed that the GW luminosity is suppressed as the mass ratio of the two stars decreases. In the post-merger phase different models show very different emission strengths, depending on very different excitation levels of the post-merger modes.

B. Properties of the models collapsing to a black hole

As previously noted, of all simulated models, two collapse to a BH. B1319+16 does so right after the merger (after about 0.98 ms). On the other hand, B1534+12 does so only after a short hypermassive neutron star (HMNS) phase, lasting around 24.2 ms. In both cases, shortly after BH formation the maximum baryonic density drops below the neutron drip threshold (see Fig. 5), and the whole dynamics of the final disk around and accreting onto the BH is described by the single-piece of the EOS with $\Gamma = 1.28733$.

For B1913+16, almost all matter quickly enters the newly formed BH within the first millisecond, to arrive at a final BH mass of $M_{\text{bh}} = 2.76 M_{\odot}$ and a dimensionless rotational parameter $a = J_{\text{bh}}/M_{\text{bh}}^2 = 0.80$. The measured values (on the numerical determined apparent horizon) of the mass (M_{bh}) and angular momentum (J_{bh})

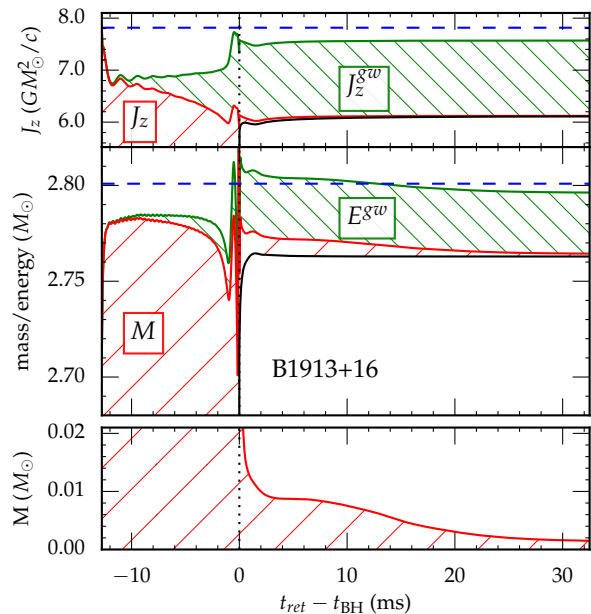


FIG. 6. Angular momentum (top-panel) and mass budget (middle-panel) for the evolution of model B1913+16. The blue, dashed, horizontal line indicates the ADM values of the initial data, as calculated by LORENE. The red-hatched area shows the matter contribution, while the green-hatched area shows the contributions from the emitted GWs, and finally, the black-solid line represents the BH contribution. The bottom panel shows the total gravitational mass of the matter present on the numerical grid, zoomed-in to highlight the late-time accretion.

do not change, within the numerical error, past 5 ms after BH formation. At the same time, the total gravitational mass present in numerical grid (outside of the horizon) is $M = 7.5, 3.0, 1.6$ ($10^{-3} M_{\odot}$) 10, 20 and 30 ms after the formation of the BH, respectively. The details of the overall dynamics concerning the energy E_{gw} and the angular momentum J_{gw} carried away by gravitational radiation and the BH formation is shown in Fig. 6. From there it also apparent that about 30 ms after BH formation the accretion dynamics has stabilized, within the time-scales considered in these simulations.

In contrast to B1913+16, B1534+12 does not show a prompt collapse, as can be seen in a similar Fig. 7. The BH formation itself also happens slower in that case. 5 ms after BH formation the BH is characterized by a $M_{\text{bh}} = 2.45 M_{\odot}$ and $a = 0.61$, and these values keep increasing to their final measured values (30 ms after BH formation) of $M = 2.49 M_{\odot}$ and $a = 0.65$. At that time, the computational grid still contains matter of total gravitational mass of $M_{\text{disk}} = 0.06 M_{\odot}$ and angular momentum $J_{\text{disk}} = 0.398 GM_{\odot}/c^2$. From this information we can deduce that the final state of the BH will be $M = 2.49 M_{\odot}$ and $a = 0.68$, since the amount of gravitational energy and angular momentum carried away by gravitational radiation from this moment on is negligible. The accretion rate $A_r = dM_{\text{bh}}/dt$ of the remnant BH

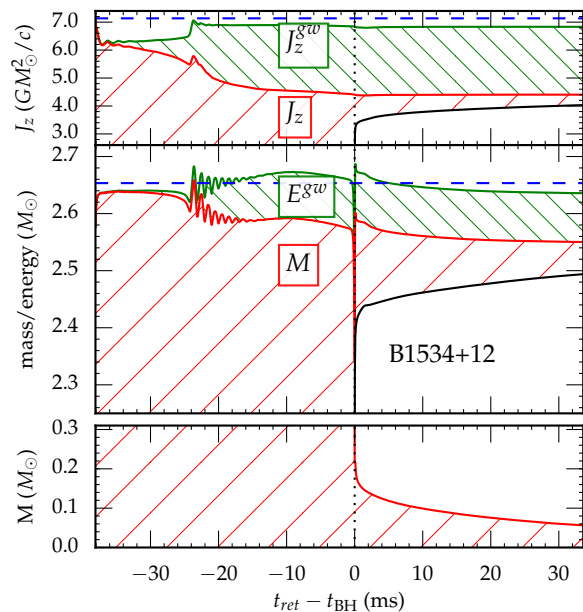


FIG. 7. Angular momentum (top-panel), mass budget (middle-panel) and total matter present in the grid (bottom-panel) for the evolution of model B1534+12. This figure is similar to Fig. 6

35 ms after BH is $\simeq 0.86 \cdot 10^{-3} M_{\odot}/\text{ms}$, is still decreasing but stabilizing.

To summarize, systems B1534+12 and B1913+16 will both collapse to a very fast rotating BH, characterized by a dimensionless rotational parameter $a = J_{\text{bh}}/M_{\text{bh}}^2$ of 0.68 and 0.80, respectively. However, B1534+12 will show a short-lived HMNS, while B1913+16 collapses promptly.

C. Effect of the EOS on the J0453+1559 ($q = 0.75$) galactic system

We study the effects of different EOSs on the recently discovered [10] BNS model associated to the pulsar J0453+1559, which is the most asymmetric known binary system, characterized by the mass ratio of $q = 0.75$. Here we analyze, as in [70], the effect of the EOS on an unequal mass BNS. In particular, we used the three additional EOSs (see Section II) APR4, H4 and MS1. The use of a different EOS changes the threshold for (following the terminology introduced by [71]) a (supra)massive neutron star (SMNS), or a (hyper)massive neutron star (HMNS), as can be seen in Tab. IV.

From this it is clear that for the J0453+1559 system, with a total conserved baryonic mass of $3.01 M_{\odot}$, the final state does not need to be a BH in the case of the MS1 EOS. Since its total baryonic mass is less than the maximum mass for a non-rotating star, it will not even be a SMNS. On the other hand, the merger remnant will be a SMNS in the case of the APR4 EOS and a HMNS in the case of the SLy and H4 EOSs, for the same baryonic

EOS	SMNS (M_{\odot})	HMNS (M_{\odot})
SLy	2.04 (2.42)	2.41 (2.82)
H4	2.01 (2.30)	2.37 (2.70)
APR4	2.19 (2.66)	2.60 (3.09)
MS1	2.75 (3.30)	3.29 (3.90)

TABLE IV. Maximum masses for a SMNS and HMNS for a set of 4 different EOSs. Quantities in brackets show the corresponding conserved baryonic mass.

EOS	τ_0 (ms)	f_0 (kHz)	f_p (kHz)	\hat{f}_p (kHz)	\hat{f} (kHz)
SLy	2.54	0.998	3.331	3.268	3.429
APR4	1.83	1.136	3.310	3.310	3.520
H4	2.79	0.992	2.439	2.359	
MS1	2.05	1.048	1.998	1.916	

TABLE V. Main peak frequencies and damping times of the post-merger phase of the simulation of the J0453+1559 system using different choices for the EOS, using a resolution of $dx = 0.25$ CU. τ_0 and f_0 are the damping time and the frequency of the oscillation of the lapse α between 1.5 to 8 ms after t_{merger} . The frequency f_p is determined by a single-frequency fitting procedure on the last part of h_{22} signal, while the other two \hat{f}_p, \hat{f} are derived by the analysis of the Fourier spectrum (bottom-right panel of Fig. 8). There are other secondary peaks but they are not reported here since they are below the LIGO/Virgo design sensitivity.

mass.

We evolved J0453+1559 for all the four EOS for about 30 ms after merger. None of these collapsed to a black hole within this time. Fig.8 (similar to Fig. 3) shows the amplitude of the $r \cdot h_{22}$ mode (GW signal, top panel) as a function of $t - t_{\text{merger}}$ while on the bottom (right side panel) we show the PSD of the effective GW $\bar{h}(f)$ as a function of the frequency in the range $[-9, +12]$ ms around merger time. The bottom left panel shows the spectrogram, using 5 ms bins, as a function of time. Contrary to Fig. 3 (different binary systems), the simulated GW signal for J0453+1559 is very different depending on the EOS. In particular, the case of the H4 EOS shows the strongest post-merger signal corroborated with the biggest peak (the dashed black one) in the PSD panel and a frequency $f_p = 2.443$ kHz (see Table II. The SLy EOS and APR4 EOS models appear very similar, although clearly recognizable, while the other two EOSs, namely the H4 EOS and the MS1 EOS look very different. Differences like these might be useful to infer information about the EOS from signals measured by interferometers like LIGO/Virgo.

The post-merger gravitational wave signal shows in all cases a quite complex evolution, especially for the first few milliseconds. The GW signal is damped, with the measured frequencies and damping times listed in Table V. These values likely directly depend on the EOS, as well as the specific merger dynamics, but this dependency cannot be quantified from the present simulations,

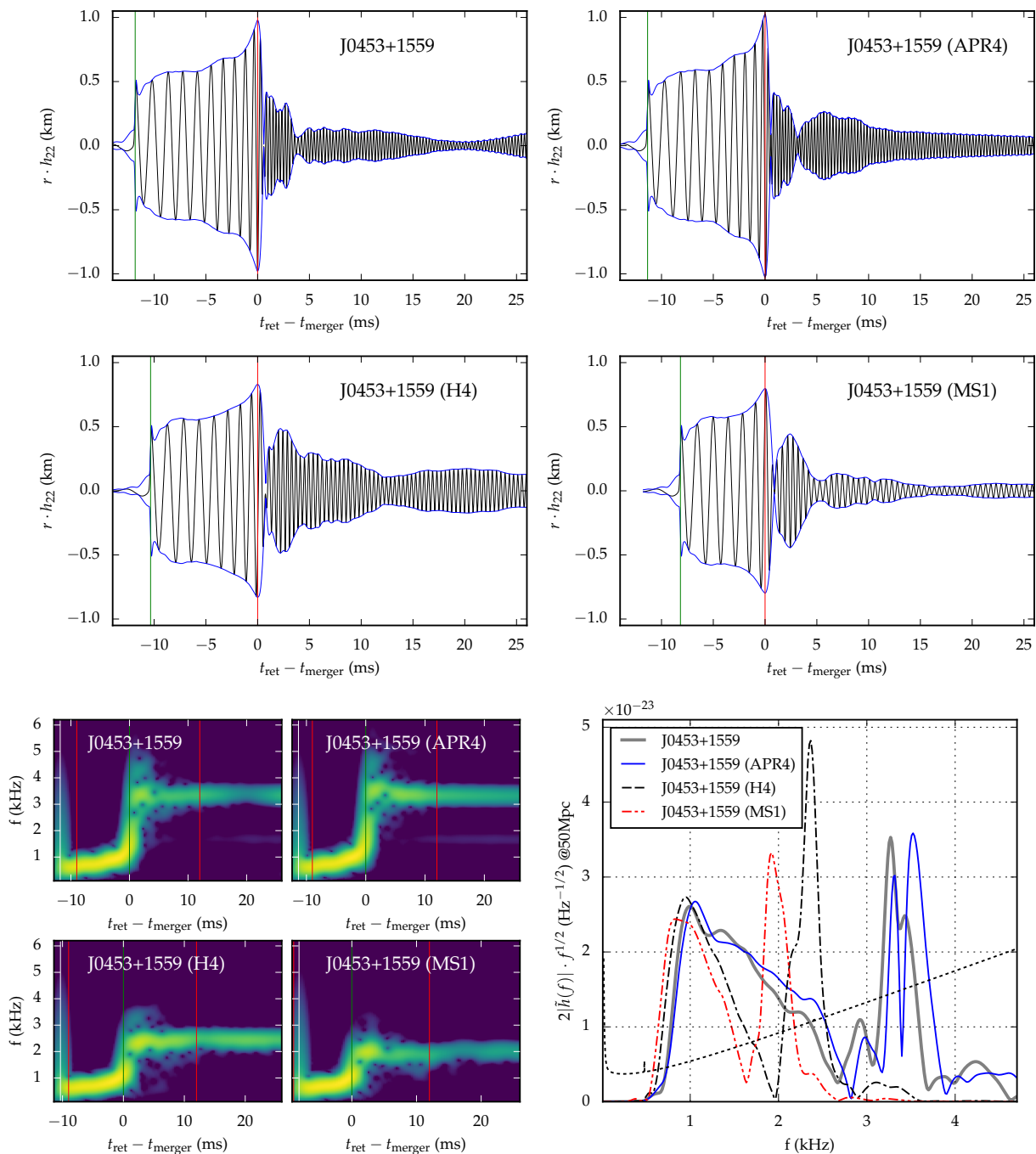


FIG. 8. Overview of the evolution of model J0453+1559 using different EOS. The meaning of plot is the same of Fig. 3. One should note the strong suppression of the side peaks of the main one and the presence of a double peaks structure of the main in the case of the SLy and APR4 EOS.

and requires further investigations. It should be noted that in some of these cases the main peak shows a split, and we denote the additional frequency as \hat{f} . In particular, for the SLy EOS this frequency corresponds to 3.429 kHz and for APR4 to 3.520 kHz (see Table V and spectrograms on the bottom-left panel of Fig. 8). The \hat{f} frequency is active during the merger phase for times comparable to the damping time τ_0 of oscillations of the

ADM lapse ($\alpha = (-g^{00})^{-1/2}$) and the maximum matter density. This effect is much stronger in the case of the APR4 EOS and is almost not present for the EOSs that correspond to less compact stars, namely stars described by the H4 and MS1 EOS, where the oscillations of the maximum density are smaller. One should also mention that this split does not show up when the masses of the two stars are almost equal.

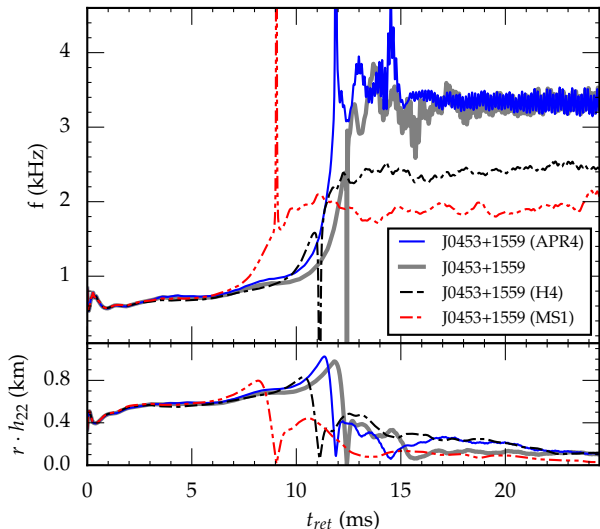


FIG. 9. Evolution of the 22 instantaneous frequency of the gravitational wave signal f (where $f(t) = d \arg(h_{22}(t))/dt$), as function of the retarded time (t_{ret}), for the J0453+1559 system, and depending on the EOS. The evolution is essentially identical for the first 5 ms, and the effect of the EOS only starts to be visible after about 7 ms.

We would also like to note that, for system J0453+1559, the GW spectrogram (bottom-left panel) shows a small signal at $f=1.67$ kHz starting at 12 ms after merger for SLy, and from 10 ms after merger in the case of the APR4 EOS, but not noticeably for the other EOSs.

In order to better understand the dynamics of the GWs emission, we show the instantaneous frequency of the h_{22} component of the GW signal, namely to the quantities $f(t) = d \arg(h_{22}(t))/dt$, in Fig. 9. We observe almost no difference between evolutions using different EOS for the first 5 ms, while after this the evolution shows a very strong influence on the EOS. As it can be seen in Table V and Fig. 8, there is a strong dependence of the frequency of the main peaks on the used EOS. The signals from SLy and APR4 show similarities also here, the signals from the other two EOSs are clearly different.

Similarly, and as shown in Fig. 10 and Table VI, while there is almost no dependence of the total energy emitted in GWs for 5 – 7 ms after merger, there are clear differences after that. The APR4 model shows the highest amount of radiated energy, while the model using MS1 shows considerably less, and also stops emitting noticeably much sooner than the other three models.

IV. CONCLUSIONS

We have presented a study of the merger of six different known galactic systems of BNSs of unequal mass

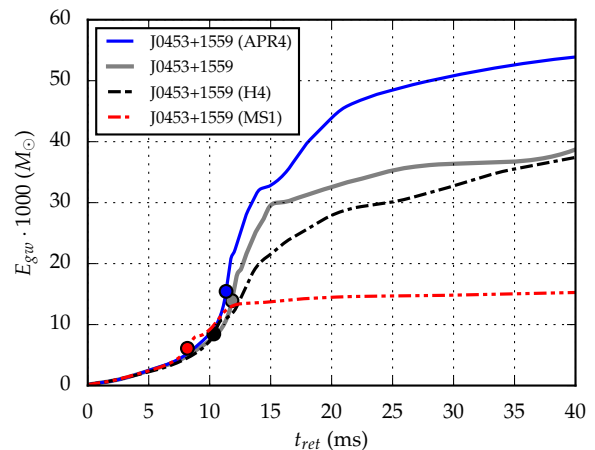


FIG. 10. Evolution of the total energy emitted in gravitational waves (E_{gw}) for the evolution of J0453+1559, as a function of the retarded time r_{ret} and depending on the used EOS. The energy is almost identical for the first 5 ms where the total energies emitted are $2.47, 2.41, 2.23,$ and $2.42 \cdot 10^{-3} M_{\odot}$ for the APR4, SLy, H4 and MS1 EOS, respectively.

EOS	E_{gw} (M_{\odot}) [...-5]	E_{gw} (M_{\odot}) [-5...5]	E_{gw} (M_{\odot}) [5...20]	t_{merger} (ms)
SLy	0.0287	0.0269	0.0060	11.8
APR4	0.0295	0.0319	0.0161	11.3
H4	0.0276	0.0197	0.0109	10.3
MS1	0.0270	0.0125	0.0012	8.17

TABLE VI. Total energy emitted as gravitational waves for system J0453+1559, from infinite separation up to 5 ms before merger (second column), from 5 ms before merger up to 5 ms after merger (third column) and from 5 ms after merger up to 20 ms after merger (forth column), for four different EOSs. The fifth column shows the merger time.

with a mass ratio between 0.75 and 0.99: J1756-2251, J0737-3039A, J1906+0746, B1534+12, J0453+1559 and B1913+16. For all of these, we used a semi-realistic, seven segment piece-wise polytropic SLyPP EOS with a thermal component of $\Gamma_{th} = 1.8$. For the most extreme of these systems ($q = 0.75$, J0453+1559), we also have investigated the effects of different EOSs, namely: APR4, H4, and MS1.

We follow the dynamics of the merger from the late stage of the inspiral process up to ~ 20 ms after the system has merged, either to form a HMNS or a rotating BH. All simulations have been performed using only publicly available, open-source codes such as, the Einstein Toolkit code deployed for the dynamical evolution, and the LORENE code for the generation of the initial models. All simulations start with the stars at a distance of 44.3 km, which corresponds to 3-4 orbits before merger, and all use a resolution of $dx = 0.25$ CU. We followed the late-inspiral phase and post-merger for more than 20 ms (in some cases up to 40 ms).

A detailed comparison with the now huge literature

(see [18, 72, 73]) on BNS systems is difficult and beyond the scope of the present work. This is particularly difficult because in most of the work full details on the numerical setting and a detailed descriptions of the EOS are lacking. Also, in most of the numerical work the crust part of the EOS is not considered or just approximated by a single polytropic EOS. In fact, in the interpretation of the results one should keep in mind that the final scenario is strongly dependent on the EOS, i.e., that the post-merger remnant may be either a (supra)massive neutron star (SMNS), a (hyper)massive neutron star (HMNS), or directly a BH surrounded by an accretion disk.

In all evolutions presented in this work, the amount of baryonic matter leaving the grid is less than $0.01 M_{\odot}$. Using the SLy EOS (in its piece-wise polytropic representation used here), of the simulated systems, J1756-2251 and J0737-3039A result in a SMNS (very close to the threshold $M_{max}^{SLy} = 2.82 M_{\odot}$ to be HMNS), while all the other correspond to HMNSs. Only two of the HMNSs collapse to a BH within the simulated time (35 ms); one right after the merger (B1913+16, Hulse-Taylor system), and the second after a short hyper massive NS phase formation of 25 ms (B1534+12). These cases have some resemblance to the already analyzed cases in [32], namely models SLy16vs16 and SLy15vs15, respectively. Both models result in a BH surrounded by an accretion disk, but with a disk of very much different mass. The final dimensionless rotational parameter of the BH ($a = J_{bh}/M_{bh}^2$) is 0.80 for B1913+16, while the expected final value for B1534+12 is 0.68.

We also considered the evolution of J0453+1559, using also three different EOSs. The remnant just after the merger is a HMNS for SLy and H4, while it is a SMNS in the case of APR4, and in the case of M1 the system is even below the non-rotating maximum mass. Nevertheless, none of these models collapses to a BH within the first 35 ms after merger. We have also shown that the inspiral phase of the merger is not very sensible to the EOS. Dominant effects should be related to the eccentricity, as shown in [33], but not studied here. Tidal effects during this phase may in principle be detected by future LIGO/Virgo/KAGRA detectors and will depend on eccentricity. Thus, it is crucial to reduce the orbital eccentricity in simulations to maximize the precision with which we can extract neutron-star parameters and constrain the neutron star EOS from GW observations. This task has already been considered in [48], and we will leave the task to find the appropriate method to generate the (still-lacking) public initial data with no eccentricity to future work.

Most of the energy in GWs is emitted during the merger (from 5 ms before to 5 ms after it). The GW signal during the inspiral is essentially identical for all models. On the other hand, the total amount of energy emitted in the post-merger (from 5 ms to 20 ms after merger) is almost of the same size as the total energy emitted during the whole inspiral phase (from infinite separation to 5 ms before merger). We note that for the more extreme

unequal mass case (J0453+1559) the total energy emitted is much reduced, in agreement with the results of Ref. [32], where it was shown that the GW luminosity is suppressed as the mass ratio of the two stars decreases. There is also the notable exception of B1913+16, which promptly collapses to a BH and shortly after stops emitting GWs. This is similar to binary black hole mergers, which would make it more difficult to discriminate this case from a BBH merger.

Finally, we would like to remark that the merger and post-merger phases show a very complicated GW pattern, stemming likely from very complex excitation mode dynamics. Because of this, we expect it to be unlikely that semi-analytic templates could be assembled to represent the full GW signal from the inspiral to the post-merger phase. The only common characteristic (beside the one from inspiral phase up to five ms before merger) seems to be that there is a final and sustained phase in the late post-merger dynamics in which there is only a dominating mode in the 22-component.

ACKNOWLEDGMENTS

This project greatly benefited from the availability of public software that enabled us to conduct all simulations, namely “LORENE” and the “Einstein Toolkit”. We do express our gratitude to the many people that contributed to their realization.

This work would have not been possible without the support of the SUMA INFN project that provided the financial support of the work of AF and the computer resources of the CINECA “GALILEO” HPC Machine, where most of the simulations were performed. Other computational resources were provided by the Louisiana Optical Network Initiative (QB2, allocations loni_hyrel, loni_numrel, and loni_cactus), and by the LSU HPC facilities (SuperMike II, allocations hpc_hyrel15 and hpc_numrel). FL is directly supported by, and this project heavily used infrastructure developed using support from the National Science Foundation in the USA (Grants No. 1212401, No. 1212426, No. 1212433, No. 1212460). Partial support from INFN “Iniziativa Specifica TEONGRAV” and by the “NewCompStar”, COST Action MP1304, are kindly acknowledged.

- [1] B. P. Abbott *et al.* (Virgo, LIGO Scientific), Phys. Rev. Lett. **116**, 061102 (2016), arXiv:1602.03837 [gr-qc].
- [2] B. P. Abbott *et al.* (Virgo, LIGO scientific), Phys. Rev. Lett. **116**, 241103 (2016), arXiv:1606.04855 [gr-qc].
- [3] B. P. Abbott *et al.* (Virgo, LIGO scientific), (2016), arXiv:1602.03840 [gr-qc].
- [4] B. P. Abbott *et al.* (Virgo, LIGO scientific), Astrophys. J. **818**, L22 (2016), arXiv:1602.03846 [astro-ph.HE].
- [5] J. Aasi *et al.* (LIGO Scientific), Class. Quant. Grav. **32**, 074001 (2015), arXiv:1411.4547 [gr-qc].
- [6] F. Acernese *et al.* (VIRGO), Class. Quant. Grav. **32**, 024001 (2015), arXiv:1408.3978 [gr-qc].
- [7] Y. Aso, Y. Michimura, K. Somiya, M. Ando, O. Miyakawa, T. Sekiguchi, D. Tatsumi, and H. Yamamoto (KAGRA), Phys. Rev. **D88**, 043007 (2013), arXiv:1306.6747 [gr-qc].
- [8] R. A. Hulse and J. H. Taylor, Astrophys. J. **195**, L51 (1975).
- [9] J. M. Weisberg, D. J. Nice, and J. H. Taylor, Astrophys. J. **722**, 1030 (2010), arXiv:1011.0718 [astro-ph.GA].
- [10] J. G. Martinez, K. Stovall, P. C. C. Freire, J. S. Deneva, F. A. Jenet, M. A. McLaughlin, M. Bagchi, S. D. Bates, and A. Ridolfi, Astrophys. J. **812**, 143 (2015), arXiv:1509.08805 [astro-ph.HE].
- [11] A. J. Faulkner *et al.*, Astrophys. J. **618**, L119 (2004), arXiv:astro-ph/0411796 [astro-ph].
- [12] M. Burgay *et al.*, Nature **426**, 531 (2003), arXiv:astro-ph/0312071 [astro-ph].
- [13] M. Kramer *et al.*, Science **314**, 97 (2006), arXiv:astro-ph/0609417 [astro-ph].
- [14] D. R. Lorimer *et al.*, Astrophys. J. **640**, 428 (2006), arXiv:astro-ph/0511523 [astro-ph].
- [15] J. van Leeuwen *et al.*, Astrophys. J. **798**, 118 (2015), arXiv:1411.1518 [astro-ph.SR].
- [16] A. Wolszczan, Nature **350**, 688 (1991).
- [17] E. Fonseca, I. H. Stairs, and S. E. Thorsett, Astrophys. J. **787**, 82 (2014), arXiv:1402.4836 [astro-ph.HE].
- [18] D. R. Lorimer, Living Reviews in Relativity **11** (2008), 10.1007/lrr-2008-8.
- [19] B. Moore, M. Favata, K. G. Arun, and C. K. Mishra, Phys. Rev. **D93**, 124061 (2016), arXiv:1605.00304 [gr-qc].
- [20] F. Douchin and P. Haensel, Astron. Astrophys. **380**, 151 (2001), arXiv:astro-ph/0111092.
- [21] J. S. Read, B. D. Lackey, B. J. Owen, and J. L. Friedman, Physical Review D **79**, 124032 (2009).
- [22] T. Nakamura, K. Oohara, and Y. Kojima, Prog. Theor. Phys. Suppl. **90**, 1 (1987).
- [23] M. Shibata and T. Nakamura, Phys. Rev. D **52**, 5428 (1995).
- [24] T. W. Baumgarte and S. L. Shapiro, Phys. Rev. D **59**, 024007 (1999), arXiv:gr-qc/9810065.
- [25] M. Alcubierre, B. Brügmann, T. Dramlitsch, J. A. Font, P. Papadopoulos, E. Seidel, N. Stergioulas, and R. Takahashi, Phys. Rev. D **62**, 044034 (2000), arXiv:gr-qc/0003071.
- [26] M. Alcubierre, B. Brügmann, P. Diener, M. Koppitz, D. Pollney, E. Seidel, and R. Takahashi, Phys. Rev. D **67**, 084023 (2003), arXiv:gr-qc/0206072.
- [27] C.-W. Shu, Lect. Not. Math. **1697**, 325 (1998).
- [28] F. Löffler, J. Faber, E. Bentivegna, T. Bode, P. Diener, R. Haas, I. Hinder, B. C. Mundim, C. D. Ott, E. Schnetter, G. Allen, M. Campanelli, and P. Laguna, Class. Quantum Grav. **29**, 115001 (2012), arXiv:1111.3344 [gr-qc].
- [29] EinsteinToolkit, “Einstein Toolkit: Open software for relativistic astrophysics,” <http://einstein toolkit.org/>.
- [30] LORENE, “LORENE: Langage Objet pour la RELativité Numérique,” <http://www.lorene.obspm.fr/>.
- [31] E.ourgoulhon, P. Grandclement, K. Taniguchi, J.-A. Marck, and S. Bonazzola, Phys. Rev. D **63**, 064029 (2001), arXiv:gr-qc/0007028.
- [32] R. De Pietri, A. Feo, F. Maione, and F. Löffler, Phys. Rev. **D93**, 064047 (2016), arXiv:1509.08804 [gr-qc].
- [33] F. Maione, R. De Pietri, A. Feo, and F. Löffler, Class. Quant. Grav. (2016), arXiv:1605.03424 [gr-qc].
- [34] A. Akmal, V. Pandharipande, and D. Ravenhall, Phys. Rev. C **58**, 1804 (1998), arXiv:nucl-th/9804027.
- [35] B. D. Lackey, M. Nayyar, and B. J. Owen, Phys. Rev. **D73**, 024021 (2006), arXiv:astro-ph/0507312 [astro-ph].
- [36] H. Muller and B. D. Serot, Phys. Rev. **C52**, 2072 (1995), arXiv:nucl-th/9505013 [nucl-th].
- [37] Cactus developers, “Cactus Computational Toolkit,” <http://www.cactuscode.org/>.
- [38] T. Goodale, G. Allen, G. Lanfermann, J. Massó, T. Radke, E. Seidel, and J. Shalf, in *Vector and Parallel Processing – VECPAR’2002, 5th International Conference, Lecture Notes in Computer Science* (Springer, Berlin, 2003).
- [39] G. Allen, T. Goodale, G. Lanfermann, T. Radke, D. Rideout, and J. Thornburg, *Cactus Users’ Guide* (2011).
- [40] E. Schnetter, S. H. Hawley, and I. Hawke, Class. Quantum Grav. **21**, 1465 (2004), arXiv:gr-qc/0310042.
- [41] E. Schnetter, P. Diener, E. N. Dorband, and M. Tiglio, Class. Quantum Grav. **23**, S553 (2006), arXiv:gr-qc/0602104.
- [42] Carpet, Adaptive Mesh Refinement for the Cactus Framework, <http://www.carpetcode.org/>.
- [43] McLachlan, “McLachlan, a public BSSN code,” <http://www.cct.lsu.edu/~eschnett/McLachlan/>.
- [44] A. Harten, P. D. Lax, and B. van Leer, SIAM review **25**, 35 (1983).
- [45] B. Einfeldt, SIAM J. Numer. Anal. **25**, 294 (1988).
- [46] A. Bauswein, H.-T. Janka, and R. Oechslin, Physical Review D **82**, 084043 (2010).
- [47] K. Hotokezaka, K. Kyutoku, H. Okawa, and M. Shibata, Phys. Rev. **D91**, 064060 (2015), arXiv:1502.03457 [gr-qc].
- [48] K. Kyutoku, M. Shibata, and K. Taniguchi, Phys. Rev. **D90**, 064006 (2014), arXiv:1405.6207 [gr-qc].
- [49] K. Hotokezaka, K. Kiuchi, K. Kyutoku, T. Muranushi, Y.-i. Sekiguchi, M. Shibata, and K. Taniguchi, Physical Review D **88**, 044026 (2013).
- [50] E. Newman and R. Penrose, J. Math. Phys. **3**, 566 (1962).
- [51] J. G. Baker, M. Campanelli, and C. O. Lousto, Phys. Rev. D **65**, 044001 (2002), arXiv:gr-qc/0104063.
- [52] K. S. Thorne, Rev. Mod. Phys. **52**, 299 (1980).
- [53] C. O. Lousto, H. Nakano, Y. Zlochower, and M. Campanelli, Phys. Rev. **D82**, 104057 (2010), arXiv:1008.4360 [gr-qc].
- [54] A. Ashtekar, C. Beetle, O. Dreyer, S. Fairhurst, B. Kr-

- ishnan, J. Lewandowski, and J. Wisniewski, *Phys. Rev. Lett.* **85**, 3564 (2000), arXiv:gr-qc/0006006 [gr-qc].
- [55] A. Ashtekar, C. Beetle, and J. Lewandowski, *Class. Quant. Grav.* **19**, 1195 (2002), arXiv:gr-qc/0111067 [gr-qc].
- [56] A. Ashtekar and B. Krishnan, *Living Rev. Rel.* **7**, 10 (2004), arXiv:gr-qc/0407042 [gr-qc].
- [57] O. Dreyer, B. Krishnan, D. Shoemaker, and E. Schnetter, *Phys. Rev. D* **67**, 024018 (2003), arXiv:gr-qc/0206008.
- [58] J. Thornburg, *Class. Quantum Grav.* **21**, 743 (2004), arXiv:gr-qc/0306056.
- [59] N. Stergioulas, A. Bauswein, K. Zagkouris, and H.-T. Janka, *Monthly Notices of the Royal Astronomical Society* **418**, 427 (2011).
- [60] A. Bauswein, N. Stergioulas, and H.-T. Janka, *Physical Review D* **90**, 023002 (2014).
- [61] A. Bauswein and H.-T. Janka, *Physical review letters* **108**, 011101 (2012).
- [62] A. Bauswein, N. Stergioulas, and H.-T. Janka, (2015), arXiv:1508.05493.
- [63] K. Takami, L. Rezzolla, and L. Baiotti, *Phys. Rev. D* **91**, 064001 (2015), arXiv:1412.3240 [gr-qc].
- [64] K. Takami, L. Rezzolla, and L. Baiotti, *Proceedings, Spanish Relativity Meeting: Almost 100 years after Einstein Revolution (ERE 2014)*, *J. Phys. Conf. Ser.* **600**, 012056 (2015).
- [65] A. L. Watts, N. Andersson, and D. I. Jones, *Astrophys. J.* **618**, L37 (2005), arXiv:astro-ph/0309554 [astro-ph].
- [66] L. Baiotti, R. De Pietri, G. M. Manca, and L. Rezzolla, *Phys. Rev. D* **75**, 044023 (2007), arXiv:astro-ph/0609473.
- [67] G. M. Manca, L. Baiotti, R. De Pietri, and L. Rezzolla, *Class. Quantum Grav.* **24**, S171 (2007), arXiv:0705.1826 [astro-ph].
- [68] R. De Pietri, A. Feo, L. Franci, and F. Löffler, *Phys. Rev. D* **90**, 024034 (2014), arXiv:1403.8066 [gr-qc].
- [69] F. Löffler, R. De Pietri, A. Feo, F. Maione, and L. Franci, *Phys. Rev. D* **91**, 064057 (2015), arXiv:1411.1963 [gr-qc].
- [70] L. Lehner, S. L. Liebling, C. Palenzuela, O. L. Caballero, E. O'Connor, M. Anderson, and D. Neilsen, (2016), arXiv:1603.00501 [gr-qc].
- [71] T. W. Baumgarte, S. L. Shapiro, and M. Shibata, *Astrophys. J.* **528**, L29 (2000), arXiv:astro-ph/9910565 [astro-ph].
- [72] L. Lehner and F. Pretorius, *Ann. Rev. Astron. Astrophys.* **52**, 661 (2014), arXiv:1405.4840 [astro-ph.HE].
- [73] L. Baiotti and L. Rezzolla, (2016), arXiv:1607.03540 [gr-qc].